Materials Today Communications 40 (2024) 110116

Contents lists available at ScienceDirect

Materials Today Communications

journal homepage: www.elsevier.com/locate/mtcomm

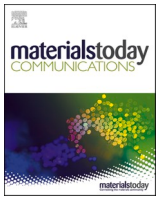

Multi-phase-field modeling of sintering applicable to solid-state and liquid-phase sintering in multiphase and multicomponent systems

Akimitsu Ishii [a,*], Toshiyuki Koyama [b], Taichi Abe [c], Michiko Ode [c]

[a] International Center for Young Scientists, National Institute for Materials Science, Tsukuba, Ibaraki 305-0047, Japan
[b] Department of Materials Design Innovation Engineering, Graduate School of Engineering, Nagoya University, Nagoya, Aichi 464-8603, Japan
[c] Computational Structural Materials Group, Research Center for Structural Materials, National Institute for Materials Science, Tsukuba, Ibaraki 305-0047, Japan

ARTICLE INFO

Keywords:
Phase-field modeling
Sintering
Multicomponent
CALPHAD

ABSTRACT

A thorough understanding and control of the microstructural evolution during sintering is essential for improving the properties of various sintered materials. In this study, a new multi-phase-field (MPF) model of sintering that applies to both solid-state sintering (SSS) and liquid-phase sintering (LPS) in multiphase and multicomponent systems was developed. The MPF model incorporates the advection term to account for the rigid-body motion (RBM) of the sintered particles. Moreover, the MPF model provides thermodynamically reasonable results of phase transformation and solute diffusion when coupled with a thermodynamic database. The effect of incorporating the RBM was validated by evaluating the neck growth and densification rates obtained from the simulation results of SSS. The MPF simulation results of the initial stage of LPS demonstrated that the a) MPF model could reproduce the densification behavior, which depends on the phase transformation between the solid and liquid phases, and b) RBM is an important factor in reproducing the densification behavior. A long-term MPF simulation of the LPS also demonstrated that the microstructural evolution, including three densification-related mechanisms—contact flattening, Ostwald ripening, and solid-state bonding—could be analyzed from the initial to final stages of the LPS. This study is expected to advance the sintering process applicable to multiphase and multicomponent systems.

1. Introduction

Polycrystalline materials, such as ceramics, metals, and cemented carbides, are fabricated by sintering, which converts powdered particles into a solid structure [1]. The properties of sintered materials depend on their microstructures, making them essential for the prediction and control of the microstructural evolution during sintering to improve the material properties. The microstructures of sintered materials are formed by complex physical phenomena and their interactions, including atomic diffusion through multiple diffusion paths, neck growth, and grain growth, resulting in the densification of the solid compact. If sintering occurs entirely in the solid state, it is called solid-state sintering (SSS). In contrast, if the compact being sintered contains liquid phases generated by the partial melting of alloys or composites, the process is called liquid-phase sintering (LPS) [2,3]. Densification is faster in LPS than in SSS because the liquid phase provides a capillary force that pulls the solid phases together. In addition, the liquid phase acts as a high-diffusivity path for atomic diffusion, thereby accelerating the densification process, and the solid particles coarsens via Ostwald ripening after the intermediate stage of LPS. The distribution of the liquid phase affects the mechanical and functional properties of functional materials. For example, the coercivity of Nd–Fe–B-based sintered magnets depends on the intergranular phase, which is formed via the solidification of the liquid phase [4,5]. Hence, a better understanding of the microstructural evolution during LPS can aid the development of materials science, engineering, and industry.

Various theoretical models have been proposed to aid the understanding of the microstructural evolution during SSS and LPS. For example, the neck growth and densification in the initial stage of sintering were modeled using a two-particle system [6–11]. The intermediate to final stages densification was modeled by considering the contributions of the lattice and grain boundary diffusions [12–14]. Ashby [15] constructed a sintering diagram from which the sintering rate and dominant mechanism could be determined for a given condition. Combined-stage theoretical models have also been developed to continuously predict the densification rate in the initial, intermediate,

* Corresponding author.
E-mail address: ISHII.Akimitsu@nims.go.jp (A. Ishii).

https://doi.org/10.1016/j.mtcomm.2024.110116
Received 3 June 2024; Received in revised form 25 July 2024; Accepted 12 August 2024
Available online 14 August 2024

and final stages [16–18]. Herring [19] developed the scaling laws that describe the sintering rate in relation to the particle size and the dominant diffusion paths. Theoretical models of the SSS and LPS have also been reviewed [1,2,20]. Although these theoretical models help to understand the SSS and LPS processes, they were derived using simplified models and assumptions, e.g., consideration of two particles only, an ideal geometry, and the use of a specific diffusion path. These assumptions limit their application in predicting the actual microstructures of sintered materials.

A numerical simulation using the phase-field (PF) method is a promising approach for predicting the microstructural evolution during sintering. Table 1 presents a summary of typical PF models of sintering [21–27] developed to date. Wang [21] developed a PF model of SSS that considers the rigid-body motion (RBM) of the sintered particles; the RBM is an important aspect of the simulation of the pore shrinkage and macroscopic densification of sintered compacts [28–30]. Wang's model has been extensively used for SSS simulations, and several PF models of SSS have been developed based on this model [31–35]. Biswas et al. [36–38] developed PF models of SSS by incorporating effects of the elastic energy, crystal grain orientation, and thermal conduction into Wang's model. Seiz [39] used Wang's model to investigate the effects of the RBM of the sintered particles on neck growth and densification. In other studies, a numerical scheme [40] and method to reduce the computational cost [41] of Wang's model were developed. As described herein, Wang's model is excellent for SSS simulations. However, the aforementioned PF models of SSS, which follow Wang's model, are only applicable to single-phase systems. In addition, although Wang's model considers four types of atomic diffusion paths (surface, grain boundary, bulk, and vapor), it does not consider the concentrations of the solute components. Therefore, Wang's and its follow up models are inapplicable to LPS as the microstructure changes with phase transformation and Ostwald ripening.

In addition to Wang's model, PF models of SSS have been developed based on the grand potential model [42]. The grand potential approach allows for accurate simulation of the driving force of the phase transformation by modeling the target phenomena using the projection of thermodynamic energies onto the grand potential space instead of the energies themselves. Hötzer et al. [22] developed a grand potential model of SSS and investigated the microstructural evolution and densification by performing three-dimensional PF simulations using ~25000 alumina particles. Greenquist et al. [23,43] developed a microstructural grand-potential-based sintering model and reported that it could simulate densification without considering RBM. These grand-potential-based models consider solute and vacancy diffusion. However, to the best of the authors' knowledge, these models have not been used for SSS in multiphase systems or for LPS. A possible reason for this is that simulating the microstructural evolution in a multiphase system requires the calculation of solute partitioning at the interface between different phases, which further complicates the PF models.

The multi-phase-field (MPF) method [44] has also been used to simulate sintering. Shi et al. [24] investigated the relationship between the RBM and shrinkage of the internal pores in SSS using a PF model developed by combining Wang's approach and the MPF method. Zhang et al. conducted a PF simulation of SSS targeting a multiphase system [25] using the MPF model with the parallel tangent law [45,46]. Hereinafter, this model is referred to as the Kim–Kim–Suzuki MPF (KKS–MPF) model. The KKS–MPF model provides thermodynamically reasonable results of the changes in the microstructure and solute concentrations using a thermodynamic database obtained from the CALculation of PHAse Diagrams (CALPHAD) method [47]. In the KKS–MPF model, the interfaces are in local equilibrium with equal diffusion potentials. Because iterative calculations are required to determine the concentration at which the diffusion potentials are equal in each phase [48,49], the KKS–MPF model has a relatively high computational cost, particularly when several phases exist in a target system. Using the KKS–MPF model, Zhang et al. [25] investigated the neck growth, phase transformation, and solute diffusion during the sintering of Fe–Cu powders. However, no MPF model can simultaneously consider phase transformation and RBM.

PF models of LPS have also been proposed. Villanueva et al. [26] developed a PF model of the LPS in a multiphase and multicomponent system comprising solid, liquid, and gas phases with three different solute components. By coupling the model with the Navier–Stokes and mass continuity equations (i.e., fluid dynamics equations), their model could accurately simulate the flow and wetting of liquid phases. However, this model considers no gain boundary between two particles om contacts, which constitutes an important aspect of sintering. Ravash et al. [27] developed a PF model of LPS and reported that it could help to analyze the three-dimensional microstructural evolution in the final stage of LPS. Their simulations targeted the final stage of LPS so that the system comprised only solid and liquid phases and did not include the gas/vapor phase. When solid phases come into contact and form grain boundaries, RBM occurs due to grain boundary diffusion in both SSS and LPS [3]. However, none of existing PF models of LPS consider this aspect. In addition, there are no PF models capable of continuously simulating the LPS process from the initial to final stages. Furthermore, from a practical perspective, there is a need for a PF model that can be used for both SSS and LPS in multiphase and multicomponent systems.

In this study, a new PF model of sintering is developed that applies to both SSS and LPS in multiphase and multicomponent systems. The PF model was developed by incorporating the RBM of the sintered particles with the finite interface dissipation (FID–MPF) proposed by Zhang and Steinbach [50,51]. The FID–MPF model can simulate the microstructural evolution with solute diffusions in multiphase and multicomponent systems using the CALPHAD database without the convergence calculations for the parallel tangent law in the KKS–MPF model. Therefore, the present computationally efficient MPF model of sintering can simultaneously analyze the phase transformation, solute diffusion, and RBM of the sintered particles. In addition, the FID–MPF-based sintering model is applicable to non-equilibrium processes, such as rapid heating and cooling (the FID–MPF model can also be referred to as a nonequilibrium MPF model [48,49]).

The remainder of this paper is organized as follows: Section 2 describes the MPF model developed in this study. Section 3 presents the simulation conditions used in the following sections. In Section 4.1, the effects of the RBM on neck growth and densification in the SSS are discussed. Section 4.2 investigates the relationship between phase transformation, densification, and RBM in LPS. Section 4.3 presents the microstructural evolution and solute diffusion occurring from the initial to final stages of LPS by performing an MPF simulation using 80 particles. Finally, Section 5 presents the conclusions of this paper.

Table 1
Representative phase-field models of sintering.

Author(s)	Sintering type	Target system	Rigid-body motion	Ref.
Wang	Solid-state sintering (SSS)	Single phase	Considered	[21]
Hötzer et al.	SSS	Single phase	–	[22]
Greenquist et al.	SSS	Single phase	–	[23]
Shi et al.	SSS	Single phase	Considered	[24]
Zhang et al.	SSS	Multiphase	–	[25]
Villanueva et al.	Liquid-phase sintering (LPS)	Multiphase	–	[26]
Ravash et al.	LPS	Multiphase	–	[27]
This work	SSS and LPS	Multiphase	Considered	

2. Multi-phase-field model

To simulate the microstructural evolution during sintering, multiple PF variables ϕ_α ($\alpha = 1, 2, \ldots, N$) were defined. ϕ_α represents the probability of the particles/phases in the target system. In this study, ϕ_α ($1 \leq$

$\alpha \le N-2$) represents solid particles. ϕ_{N-1} and ϕ_N are the liquid and gas phases, respectively. The present model treats the pores and outer parts of the sintered compact as the gas phase. Although this definition allows for phase transformations between the solid and gas phases or between liquid and gas phases, it maintains the thermodynamic consistency of the formulations in the MPF model. Each particle was assumed to be a single crystal. Thus, the interface between the particles was considered to be the grain boundary. ϕ_α changes smoothly from zero to one at the interface and satisfies the following constraint:

$$\sum_{\alpha=1}^{N} \phi_\alpha = 1 \tag{1}$$

Additionally, c^i ($i = 1, 2, \ldots, N_c$) is defined as the molar fraction of the solute component used to analyze the time evolution of the concentration fields. c^i is expressed as follows:

$$c^i = \sum_{\alpha=1}^{N} \phi_\alpha c_\alpha^i \tag{2}$$

where c_α^i is the local molar fraction of the ith component of the αth phase. The total free energy of system G is defined as [50,51]

$$G = \int_V \left[\begin{array}{l} \displaystyle\sum_{\alpha=1}^{N} \sum_{\beta=\alpha+1}^{N} \left(W_{\alpha\beta}\phi_\alpha\phi_\beta \right) + \sum_{\alpha=1}^{N} \sum_{\beta=\alpha+1}^{N} \left(-\frac{\varepsilon_{\alpha\beta}^2}{2} \nabla\phi_\alpha \cdot \nabla\phi_\beta \right) \\ \displaystyle + \sum_{\alpha=1}^{N} \left(\phi_\alpha \frac{G_\alpha}{V_m} \right) + \sum_{i=1}^{N_c-1} \lambda^i \left\{ c^i - \sum_{\alpha=1}^{N} \left(\phi_\alpha c_\alpha^i \right) \right\} \end{array} \right] dV, \tag{3}$$

where V_m denotes the molar volume of the material. $W_{\alpha\beta}$ and $\varepsilon_{\alpha\beta}$ are the height of the double-obstacle potential and gradient energy coefficient at the interface between the αth and βth phases, respectively. λ^i is a Lagrange multiplier used to ensure the relationship expressed in Eq. (2). G_α is the molar Gibbs free energy of the αth phase obtained from the CALPHAD database. $W_{\alpha\beta}$ and $\varepsilon_{\alpha\beta}$ can be expressed as follows:

$$W_{\alpha\beta} = \frac{4\sigma_{\alpha\beta}}{\delta} \tag{4}$$

and

$$\varepsilon_{\alpha\beta} = \frac{2}{\pi}\sqrt{2\delta\sigma_{\alpha\beta}}, \tag{5}$$

where δ and $\sigma_{\alpha\beta}$ denote the interface thickness and interfacial energy between the αth and βth phases, respectively.

The time evolution of c^i can be indirectly calculated using Eq. (2) with ϕ_α and c_α^i [52]. The evolution equation for c_α^i is given as follows [50–52]:

$$\frac{\partial c_\alpha^i}{\partial t} = \frac{P^i}{V_m} \sum_{\beta=1}^{N} \phi_\beta \left(\mu_\beta^i - \mu_\alpha^i \right) - \sum_{\beta=1}^{N} \frac{\partial \phi_\beta}{\partial t} \left(c_\beta^i - c_\alpha^i \right) + \nabla\cdot \left[\sum_{\beta=1}^{N} \left\{ \phi_\beta \sum_{j=1}^{N_c-1} \left(D_\beta \nabla c_\beta^j \right) \right\} \right] \tag{6}$$

where μ_α^i is the diffusion potential and is expressed as $\mu_\alpha^i = \partial G_\alpha / \partial c_\alpha^i$. P^i is a kinetic coefficient, referred to as the permeability, that governs the partitioning of the ith solute component at the interface. The greater the P^i value is, the closer the change in c_α^i simulated by the FID–MPF model is to that simulated by the KKS–MPF model. D_β is a coefficient correlated with solute diffusion. Because atomic diffusion at the grain boundaries affects the microstructural evolution during sintering, the diffusivity at the grain boundaries is explicitly set to be high by defining D_β as follows:

$$D_\beta = D_\beta^{ij} + \sum_{\gamma>\beta}^{N-2} \xi^{ij} \phi_\beta \phi_\gamma, \tag{7}$$

where D_β^{ij} denotes the chemical diffusivity of the βth phase, and ξ^{ij} is a parameter used to enhance the diffusion at the grain boundary between the βth and γth phases.

The time evolution equation of ϕ_α can be expressed as

$$\frac{\partial \phi_\alpha}{\partial t} = -\frac{2}{N} \sum_{\beta=1}^{N} M_{\alpha\beta}^{\phi} \left(\frac{\partial G}{\partial \phi_\alpha} - \frac{\partial G}{\partial \phi_\beta} \right) - \nabla\cdot\mathbf{v}_\alpha, \tag{8}$$

where $M_{\alpha\beta}^{\phi}$ is the PF mobility, defined as $M_{\alpha\beta}^{\phi} = (\pi^2/8\delta) M_{\alpha\beta}$. Here, $M_{\alpha\beta}$ is the interfacial mobility between the αth and βth phases, and $\boldsymbol{v}_\alpha$ denotes the advection velocity of the αth phase. The first term on the right side of Eq. (8) is a common term in MPF models, whereas the second term is the advection velocity term used to analyze the RBM of the sintered particles that occurs when the particles are in contact. By substituting Eq. (3) into Eq. (8), the time evolution equation of ϕ_α can be expressed as follows:

$$\frac{\partial \phi_\alpha}{\partial t} = -\frac{2}{N} \sum_{\beta=1}^{N} M_{\alpha\beta}^{\phi} \left[\sum_{\gamma=1}^{N} \left\{ \left(W_{\alpha\gamma} - W_{\beta\gamma} \right) \phi_\gamma + \frac{1}{2} \left(\varepsilon_{\alpha\gamma}^2 - \varepsilon_{\beta\gamma}^2 \right) \nabla^2 \phi_\gamma \right\} + \Delta g_{\alpha\beta} \right] - \nabla\cdot\mathbf{v}_\alpha \tag{9}$$

where $\Delta g_{\alpha\beta}$ is the chemical driving force and can be described as follows:

$$\Delta g_{\alpha\beta} = \frac{G_\alpha}{V_m} - \frac{G_\beta}{V_m} - \sum_{i=1}^{N_c-1} \left\{ \sum_{\alpha=1}^{N} \left(\phi_\alpha \frac{\mu_\alpha^i}{V_m} \right) + \frac{1}{P^i} \sum_{\alpha=1}^{N} \left(\phi_\alpha \frac{\partial c_\alpha^i}{\partial t} \right) \right\} \left(c_\alpha^i - c_\beta^i \right). \tag{10}$$

During sintering, the necks grow between the contacting particles. When the dominant factor influencing neck growth is grain boundary diffusion, vacancies are oversaturated at the grain boundaries. The annihilation of these oversaturated vacancies by dislocations leads to RBM, which drives the macroscopic densification of a sintered compact [1,21]. Because the MPF model considers the concentration field, the most thermodynamically reasonable approach for calculating the advection velocity is to analyze the vacancy diffusion and solute components simultaneously. However, in contrast to atoms, vacancies should be strictly treated as nonconserved variables, leading to further complications in the MPF model. This can also make it difficult to prepare a CALPHAD database. Therefore, in this MPF model, the advection velocity was calculated based on Wang's approach [21], which requires no explicit consideration of the vacancy concentration. When the αth phase represents a solid particle, $\boldsymbol{v}_\alpha$ can be calculated as follows:

$$\boldsymbol{v}_\alpha = \boldsymbol{v}_\alpha^{\mathrm{tr}} + \boldsymbol{v}_\alpha^{\mathrm{ro}} \quad (\alpha \le N-2), \tag{11}$$

where $\boldsymbol{v}_\alpha^{\mathrm{tr}}$ and $\boldsymbol{v}_\alpha^{\mathrm{ro}}$ are the transrational and rotational velocities of the αth particle, respectively. Additionally, $\boldsymbol{v}_\alpha^{\mathrm{tr}}$ is expressed as

$$\boldsymbol{v}_\alpha^{\mathrm{tr}} = \frac{m^{\mathrm{tr}}}{V_\alpha} \boldsymbol{F}_\alpha \phi_\alpha, \tag{12}$$

where V_α is the volume of the αth particle, m^{tr} is the transrational mobility, and $\boldsymbol{F}_\alpha$is the force acting on the αth particle. Furthermore, $\boldsymbol{v}_\alpha^{\mathrm{ro}}$ is expressed by the following equation:

$$\boldsymbol{v}_\alpha^{\mathrm{ro}} = \frac{m^{\mathrm{ro}}}{V_\alpha} \boldsymbol{T}_\alpha \times [\boldsymbol{r} - \boldsymbol{r}_\alpha] \phi_\alpha, \tag{13}$$

where m^{ro} is the rotational mobility, $\boldsymbol{r}$ is the position vector, and $\boldsymbol{r}_\alpha$ is the center of the αth particle. $\boldsymbol{T}_\alpha$ is the torque acting on the αth particle. $\boldsymbol{F}_\alpha$ is expressed as

$$\boldsymbol{F}_\alpha = \int_V d\boldsymbol{F}_\alpha, \tag{14}$$

where $d\boldsymbol{F}_\alpha$ is the local force density, defined as follows:

$$d\boldsymbol{F}_\alpha = k \left\{ \left(\sum_{\beta}^{N-2} \phi_\beta - 1 \right) \sum_{\beta\neq\alpha}^{N-2} \langle \phi_\alpha \phi_\beta \rangle \left(\left. \frac{\partial \phi_\alpha}{\partial t} \right|_0 + \left. \frac{\partial \phi_\beta}{\partial t} \right|_0 \right) \left(\nabla\phi_\alpha - \nabla\phi_\beta \right) \right\} d^3\boldsymbol{r}, \tag{15}$$

where k is a parameter that controls the force magnitude. $|_0$ indicates that the term does not include the advection effect. Eq. (15) is derived under the assumption that grain boundary diffusion is a consistently dominant factor influencing neck growth. The operation $\langle \phi_\alpha \phi_\beta \rangle$ is defined as follows:

$$\langle \phi_\alpha \phi_\beta \rangle = \begin{cases} 1 & (\phi_\alpha \phi_\beta \geq C) \\ 0 & (\phi_\alpha \phi_\beta < C) \end{cases} \tag{16}$$

where C is the threshold value for identifying the grain boundary regions. $\boldsymbol{T}_\alpha$ is given by

$$\boldsymbol{T}_\alpha = \int_V (\boldsymbol{r} - \boldsymbol{r}_\alpha) \times d\boldsymbol{F}_\alpha, \tag{17}$$

where "×" denotes the outer product. When the αth phase represents a liquid or gas phase, $\boldsymbol{v}_\alpha$ is calculated as follows:

$$\boldsymbol{v}_\alpha = -\frac{\phi_\alpha}{\phi_{N-1} + \phi_N} \sum_{\beta=1}^{N-2} \boldsymbol{v}_\beta \quad (\alpha \geq N-1). \tag{18}$$

Eq. (18) maintains the widths of the interfaces between the solid–liquid and solid–gas phases. Notably, because this paper focused on implementing the RBM that occurs when the solid particles are in contact, the implementation of the advection velocity for the liquid and gas phases was simplified. For a more accurate analysis of the RBM, it is necessary to couple the MPF model with the Navier–Stokes and mass continuity equations.

The developed MPF model includes an advection term in the time evolution equation of ϕ_α (Eq. (9)) but not in the time-evolution equation of c_α^i (Eq. (6)). This is because the advection effect is reflected in the time evolution of c^i by simply including the advection term only in Eq. (9). Further details are provided in Appendix A. The PF simulations were performed using proprietary source codes developed in-house. To calculate the time evolutions of ϕ_α and c_α^i, Eqs. (6) and (9) were discretized using the finite difference method (FDM). The first-order Euler FDM was used for time integration, and the second-order central FDM was used for spatial discretization.

3. Conditions

The molar Gibbs free energy G_α is defined using the regular-solution model, according to the following equation:

$$G_\alpha = \sum_{i=1}^{N_c} \left\{ c_\alpha^i \, {}^0G_\alpha^i + RT\left(c_\alpha^i \ln\left(c_\alpha^i\right)\right) \right\} + G_\alpha^{ex}, \tag{19}$$

where R is the gas constant, T is the absolute temperature, and ${}^0G_\alpha^i$ is the molar Gibbs energy of the ith solute component in the αth phase. G_α^{ex} is the excess Gibbs energy of the αth phase. In this study, a hypothetical ternary system with elements A, B, and C, as in a previous study [26], was used to facilitate the validation of the developed MPF model, and ${}^0G_\alpha^i$ and G_α^{ex} were determined from the CALPHAD database reported in the literature [26]. Fig. 1 shows the calculated phase diagram of the A–B–C ternary system at $T = 1800$ K. The equilibrium compositions $c^{e,i}$ in the solid, liquid, and gas phases are $(c^{e,A}, c^{e,B}, c^{e,C}) = (0.07, 0.69, 0.24)$, (0.50, 0.26, 0.24), and (0.03, 0.04, 0.93), respectively.

The molar volume was set to $V_m = 1.0 \times 10^{-5}$ m^3/mol, and the finite-difference grid size was $\Delta l = 10$ nm. The time evolution equations were nondimensionalized using Δl and the energy density RT/V_m. The dimensionless parameters used in this study are listed as follows (the superscript * denotes the dimensionless parameter): the width of the diffuse interface was $\delta^* = 5$, the time increment was $\Delta t^* = 0.002$, all the interfaces were assumed to have the same mobility $M_{\alpha\beta}^* = 0.5$, the translational mobility was $m^{tr^*} = 500$ [21], the rotational mobility was $m^{ro^*} = 1$ [21], the control parameter was $k^* = 250$, and the threshold value was $C = 0.14$ [21]. In the FID–MPF model, the solute partitioning rate was determined using P^i. Sintering is a high-temperature process in which atoms sufficiently diffuse to achieve a local equilibrium at the interface. Therefore, this study used $P^{A^*} = P^{B^*} = 1.0$, which is a sufficiently high value, such that the concentration distribution at the interface is unaffected by the partitioning rate (see Appendix B). The interfacial energies of the solid–solid interface σ_{SS}, solid–liquid interface σ_{SL}, solid–gas interface σ_{SG}, and liquid–gas interface σ_{LG} were set according to the following ratios: $\sigma_{SS}/\sigma_{SL} = 2$, $\sigma_{SG}/\sigma_{SS} = 3$, and $\sigma_{LG}/\sigma_{SG} = 0.8$ [53,54]. σ_{SS} and σ_{SG} correspond to the surface and grain boundary energies, respectively. In general, MPF models reproduce theoretically reasonable dihedral angles between interfaces calculated from interfacial energies (i.e., surface tensions). Therefore, using the above settings of interfacial energy, the MPF model of sintering can simulate the penetration of the liquid phase into the grain boundary. The diffusivities were set to $D_S^{A^*} = D_S^{B^*} = 1$, $D_L^{A^*} = D_L^{B^*} = 10$, and $D_G^{A^*} = D_G^{B^*} = 100$. Although the ratio of the diffusivities of the solid, liquid, and gas phases is generally significantly greater than the above values, these values were used in the current simulation for computational stability. The parameter enhancing the grain boundary diffusion was $\xi^{ij^*} = 4$. Notably, all the material parameter values were assumed because a hypothetical material was used in the simulation. Periodic boundary conditions were applied to the computational domain. Although the developed PF model is capable of being used for three-dimensional simulations, the previous studies have demonstrated that two-dimensional simulations are sufficient to confirm that the PF model can accurately reproduce the sintering behaviors occurring in both SSS and LPS. Therefore, in this study, two-dimensional simulations were performed to conserve computational time.

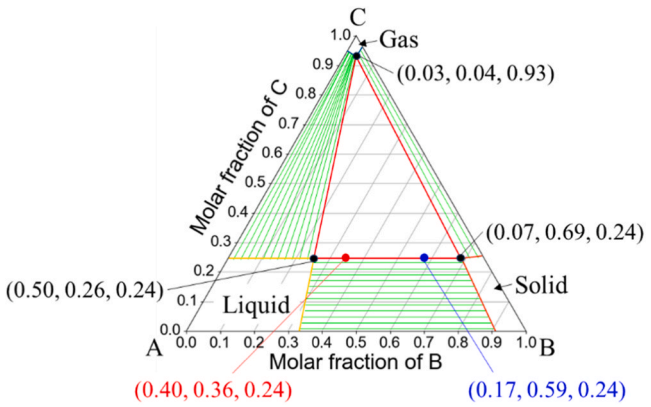

Fig. 1. Calculated phase diagram of a hypothetical A–B–C ternary system. The black points indicate the equilibrium composition of each phase. The red and blue points indicate the initial compositions of the liquid and solid phases used for Cases 2 and 3 in Section 4.2, respectively.

4. Results and discussion

4.1. Validation of rigid-body motion in solid-state sintering

As described in the Introduction section, the RBM is an important aspect of the simulation of the densification of sintered compacts. Therefore, the MPF model developed in this study must be able to analyze the RBM at least as accurately as the PF model used in the previous studies. To validate the effect of the RBM calculated using the developed MPF model, the neck growth rate was investigated based on the two-dimensional MPF simulation result of the SSS using two solid particles. The particle radius was $r = 0.2$ μm. The outer parts of the particles were in the gas phase, and no liquid phase was present in the domain. The computational domain was uniformly divided into 128^2 finite difference grids to ensure a resolution high enough to accurately solve the governing equations, with the aforementioned finite-difference

grid size Δl. Each phase was initially at the equilibrium composition. An MPF simulation without the RBM was performed to clarify the effects of the RBM by comparing the findings in the two cases.

Fig. 2(a) and (c) show the time evolution of the sintered particles obtained from the MPF simulations with and without the RBM, respectively. Fig. 2(b) shows the change in the distribution of c^B as a representative of the concentration field in the results shown in Fig. 2(a). When the RBM was considered, neck growth was accelerated. The concentration field followed the sintered particles that migrated during the RBM, and there was no deviation between the solid-phase position and the concentration distribution. The neck growth rate can be expressed by the equation: $(X^*/D^*)^n = K^*(t^* - t_0^*)$, where X^* and D^* are the neck length and particle diameter, respectively. K^*, t_0^*, and n are the fitting parameters, with n being particularly important because it reflects the dominant sintering mechanism [21]. Wang reported that a PF simulation of the SSS considering the RBM and all four diffusion paths yielded $n = 6.99$ [21]. Fig. 3 shows the neck growth rate calculated from the simulation results shown in Fig. 2(a) and (c). The simulation results with the RBM yielded $n = 6.94$, which is comparable to that reported by Wang. However, in the absence of the RBM, $n = 4.16$. These results demonstrated that the developed MPF model of sintering can help analyze the neck growth accelerated by the RBM with an accuracy comparable to that of Wang's model.

The RBM affects the shrinkage and densification of sintered compacts [39]. Thus, the effects of RBM on the macroscopic densification in the SSS were investigated by performing simulations with numerous particles. In a square computational domain with 2.56 μm sides, 80 circular particles with a radius range of 0.10–0.15 μm were randomly arranged such that each particle was in contact with at least one other. Fig. 4 shows the microstructural evolution during the SSS obtained from the MPF simulations with (Fig. 4(a)) and without (Fig. 4(b)) the RBM. The RBM accelerated the annihilation of pores inside the sintered compact, as reflected in the accelerated neck growth process. This acceleration in the pore annihilation occurred regardless of the initial particle distribution and number of particles, as demonstrated by the MPF simulations shown in Fig. 5, where the domain size and number of

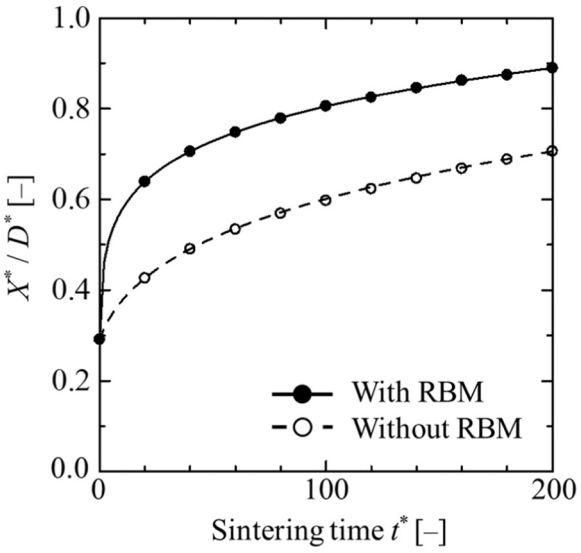

Fig. 3. Neck growth rate obtained from the multi-phase-field simulation results shown in Figs. 2(a) and 2(c).

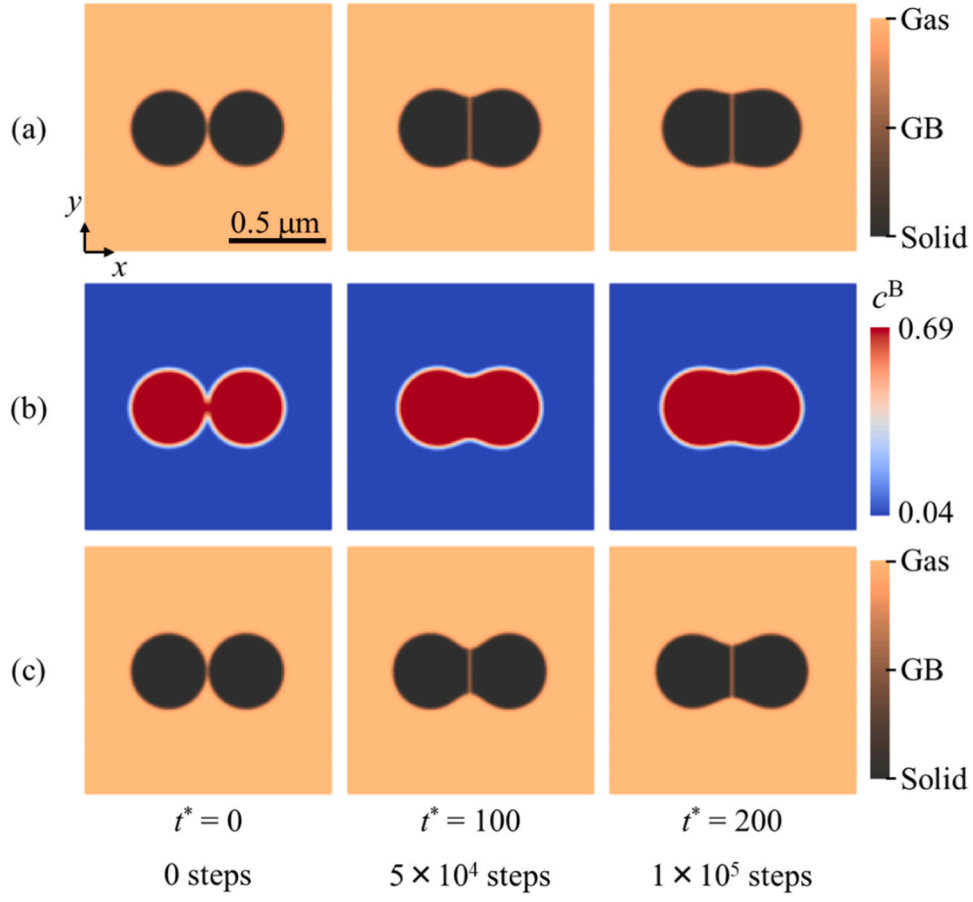

Fig. 2. Time evolution of (a) solid particles and (b) distribution of c^B obtained from the simulation with rigid-body motion (RBM). The simulation results shown in (c) did not consider RBM.

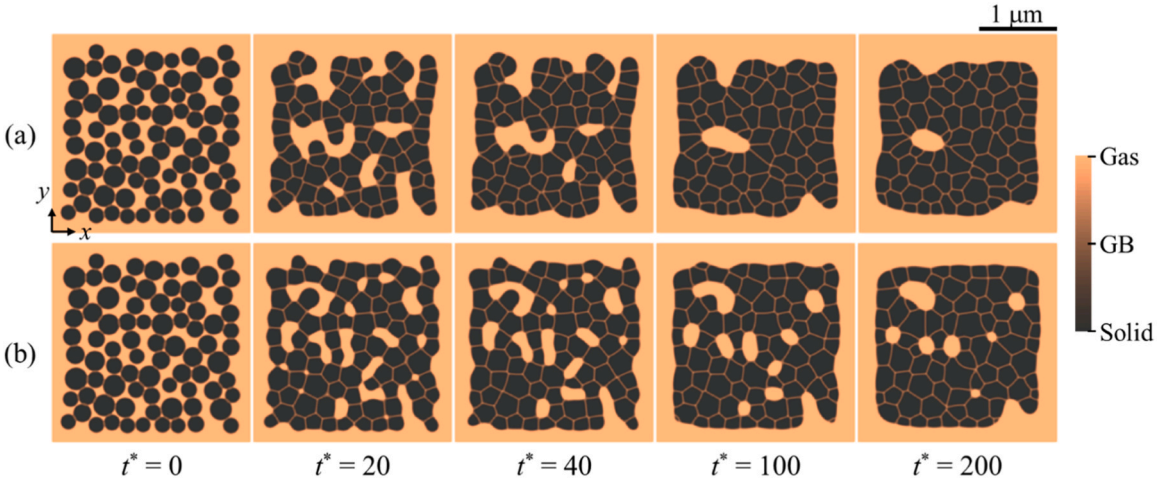

Fig. 4. Microstructural evolution during solid-state sintering using 80 particles (a) with and (b) without rigid-body motion.

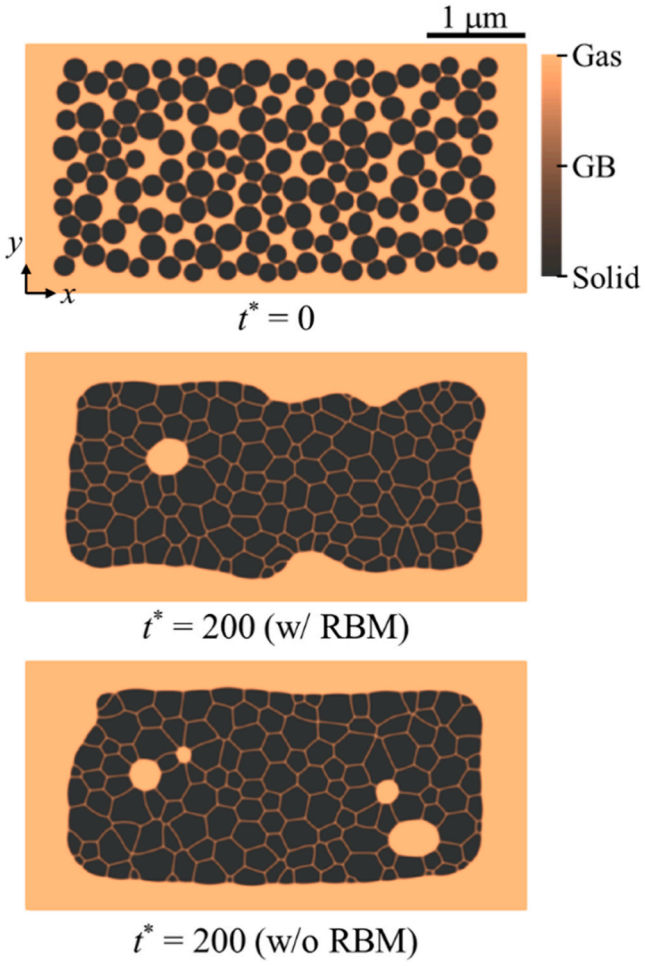

Fig. 5. Microstructures obtained from the multi-phase-field simulations of solid-state sintering using 160 particles with and without rigid-body motion (RBM).

particles are twice those in Fig. 4.

The relative densities of the sintered compacts were evaluated using the simulation results. In this study, the relative density ρ is defined as $\rho = (V_S + V_L)/(V_S + V_L + V_{G\_in}) \times 100$ [%], where V_S and V_L denote the total volumes of the solid particles and liquid phases, respectively. V_{G_in} denotes the total volume of the isolated gas phase inside the sintered compact (i.e., the total volume of the pores). If $V_{G\_in} = 0$, the relative density is $\rho = 100$ %. Fig. 6 shows the variations in the relative density as a function of the sintering time, calculated from the MPF simulation results shown in Figs. 4 and 5. Evidently, the acceleration in pore annihilation when considering the RBM was quantitatively demonstrated to lead to an increase in the densification rate. Particularly noteworthy is the relationship between the densification rate and the number of particles. When the RBM was not considered, the densification rate depended on the number of particles. However, according to the theoretical model [16], densification was independent of compact size. Seiz [39] reported that in the PF simulations of SSS using Wang's model, the densification rate is independent of the compact size only if the RBM is considered. The MPF model of sintering developed in this study also eliminates the dependence of the densification rate on the compact size by considering the RBM with an advection term. The results demonstrate that it is essential to consider the RBM of the particles to simulate the sintering behavior based on the MPF approach; in this respect, the MPF model developed in this study is effective for an accurate prediction of SSS.

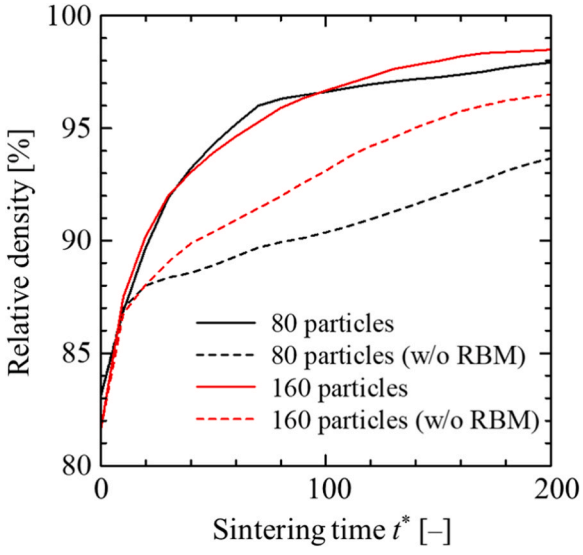

Fig. 6. Variation in the relative density with respect to the sintering time calculated from the four multi-phase-field simulation results of solid-state sintering. (RBM: rigid-body motion).

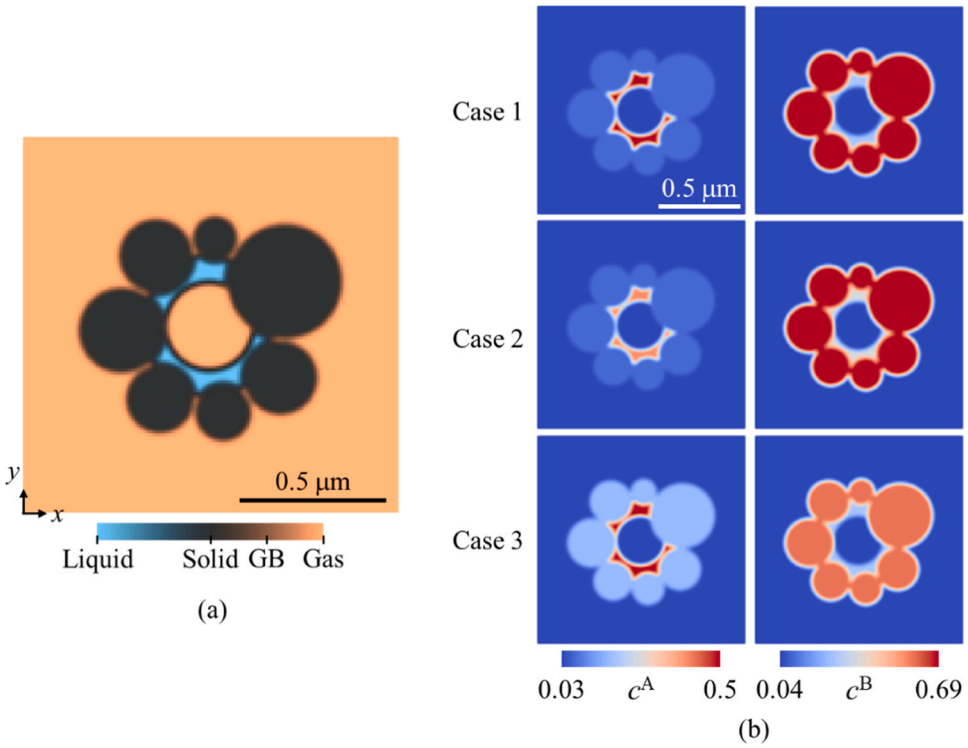

Fig. 7. Initial distributions of (a) phases and (b) concentrations of the solute components A and B. Because the initial distribution of c^C was uniform in the solid and liquid phases in all the tested cases, it was omitted.

4.2. Validation of densification in liquid-phase sintering

The densification rate in the initial stage of the LPS depends on the phase transformation behavior between the solid and liquid phases owing to the initial composition and sintering temperature. In this study, this relationship is referred to as the solid–liquid solubility relations [3]. The phase transformation rate (in other words, relative phase growth rate) from liquid to solid is denoted by S_S, the rate in the opposite direction is denoted by S_L, and their ratio can be expressed as $S = S_S/S_L$. Densification occurs when $S > 1$, and swelling occurs when $S < 1$ [2]. In this section, the developed MPF model of sintering is validated in terms of reproducing the solid–liquid solubility relations.

Fig. 7 shows the initial distributions of the phases and concentrations used in the MPF simulations to investigate the solubility relations. Seven particles with radii in the range of 0.08–0.20 μm were arranged in a circular manner. Each particle was initially in contact with its neighbors as well as the liquid phase. A pore was located at the center of the computational domain. Three simulations were conducted with different initial compositions for the same initial arrangement of the phases. In Case 1, both the solid and liquid phases were initially in equilibrium compositions; this will unlikely lead to a phase transformation, thus $S \approx 1$. In Case 2, the initial composition of the liquid phase was $(c^A, c^B, c^C) = (0.40, 0.36, 0.24)$, while the initial composition of the solid phase was its equilibrium composition. Under these conditions, $S > 1$, given the occurrence of liquid-to-solid transformation. In contrast, in Case 3, the initial composition of the solid phase was $(c^A, c^B, c^C) = (0.17, 0.59, 0.24)$ and that of the liquid phase was its equilibrium composition; therefore, $S < 1$. In all the cases, the initial composition of the gas phase was the equilibrium composition. Because the solid particles were in contact with each other, the RBM would likely affect the densification process. Therefore, MPF simulations without the RBM were also performed in all the three tested cases.

Fig. 8 shows snapshots of the microstructural evolution in the three tested cases. Although the advection term corresponding to the liquid phase was implemented in a simplified manner, as described in Section 2, the volumetric changes in the liquid phase in Cases 2 and 3 were consistent with those predicted from the phase diagram. Regardless of the RBM, in Case 1, the pores shrank with gas-to-liquid transformation. This reduced the total free energy of the system by decreasing the liquid–gas interface area. This behavior can be attributed to the assumption that the pore was treated as a gas phase was. However, a comparison of the results with and without RBM showed that the presence of RBM accelerated the shrinkage of the pores in LPS and SSS. In Case 2 with the RBM, the pores were annihilated by $t^* = 40$, with a reduction in the liquid volume owing to liquid-to-solid transformation. In Case 3 (wherein RBM was considered), the liquid phase penetrated the grain boundaries through the interaction of the solid-to-liquid transformation and the capillary effect. The penetrated liquid phase separated the solid contacts, thus increasing particle distance and swelling. Consequently, a significant difference in pore size was observed when the RBM was considered. In contrast, the results of the MPF simulations without the RBM showed no significant differences in the pore sizes among Cases 1–3, even though a phase transformation occurred between the solid and liquid phases in Cases 2 and 3.

Fig. 9 shows the variations in the relative densities. The densification rate was the highest in Case 2 with $S > 1$ and lowest in Case 3 with $S < 1$, which is consistent with the previous knowledge of the solid–liquid solubility relations [2,3]. Although this trend was observed even in the absence of RBM, the presence of RBM enhanced the difference in the densification rate owing to the changes in S. This could be attributed to the interaction between the advection effect and changes in the contact states between the solid particles or solid–liquid phases through phase

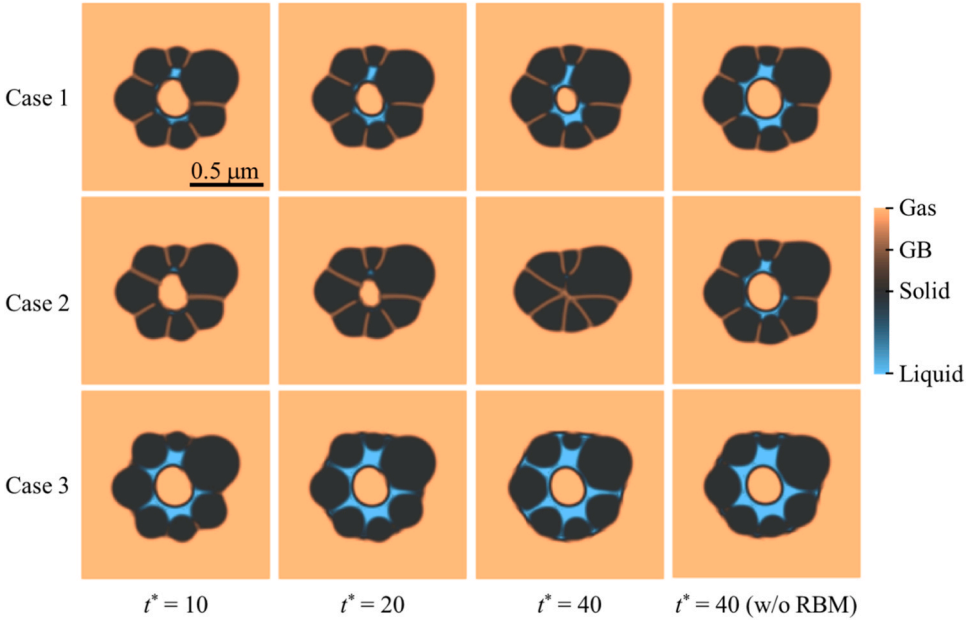

Fig. 8. Snapshots of microstructural evolutions in the three cases studied. Cases 1, 2, and 3 correspond to $S \approx 1$, $S > 1$, and $S < 1$, respectively (S denotes the ratio of the liquid-to-solid and solid-to-liquid transformation rates). The figures in the far right column show the results obtained from the multi-phase-field simulations (wherein rigid-body motion was not considered).

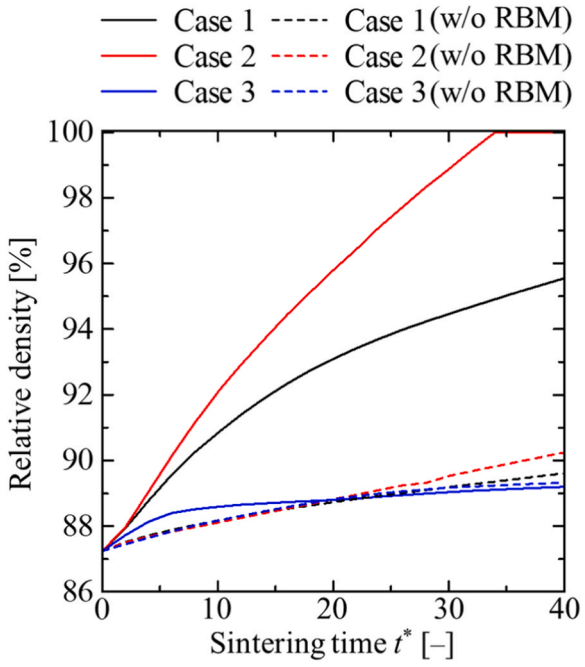

Fig. 9. Variation in the relative density with respect to the sintering time calculated from the multi-phase-field simulation results for the initial stage of liquid-phase sintering. (RBM: rigid-body motion).

transformation. The result of Case 3 with the RBM helps the understanding of the relationship between the densification rate S and the RBM. The densification rate in Case 3 (wherein RBM was considered) was significantly lower than those in Cases 1 and 2 (wherein RBM was considered) and comparable to that in Case 3 (wherein RBM was not considered). This can be attributed to the fact that the RBM no longer worked after the solid contacts were separated by the penetration of the liquid phase into the grain boundary. These results demonstrated that the MPF model of sintering could reasonably simulate the densification process by considering the solubility relationships. Furthermore, it was clarified that the RBM must be incorporated into the MPF model to explicitly describe the solubility relations in the initial stage of the LPS.

4.3. *Liquid-phase sintering simulation from the initial to final stages*

A long-term MPF simulation was performed to demonstrate the capability of the developed MPF model to continuously simulate the LPS from the initial to final stages. The computational domain contained 80 particles in the same arrangement as that described in Section 4.1, and 10 liquid phases with radii in the range of 0.04–0.06 μm were additionally arranged in the domain. The initial compositions of the solid and liquid phases were both $(c^A, c^B, c^C) = (0.15, 0.75, 0.10)$, and that of the gas phase was the equilibrium composition. The phase diagram shown in Fig. 1 indicates that this initial concentration yields $S > 1$, which results in rapid densification.

Fig. 10 shows the microstructural evolution during the MPF simulation. The liquid-phase evolution and grain boundary migration in the initial to final stages were continuously simulated. Fig. 11 shows the variation in the relative density of the sintered compact from $t^* = 0$–200. For comparison, the densification curve obtained from the SSS simulation shown in Fig. 6 is also presented. The densification rate of LPS was higher than that of SSS, and the relative densification was 100 % at $t^* = 100$. In the following discussion, the period $t^* = 0$–40 is distinguished as the initial stage, in which the densification rate is particularly high. Because it is difficult to determine the boundary between the intermediate and final stages based on the simulation results, the initial and intermediate-to-final stages are discussed. In the initial stage, SSS occurred when the particles were in contact with each other, whereas the liquid phases grew, wetted the particle surfaces, penetrated the grain boundaries by the capillary effect, and separated the solid contacts. As observed in the microstructure at $t^* = 40$, contact flattening was reproduced, in which the solid surface was flattened by the penetration of the liquid phase into the grain boundary with the solid-to-liquid transformation. In the intermediate-to-final stage, the relatively small particles isolated in the liquid phase dissolved and larger particles coarsened through solute diffusions in the liquid phase; that is, Ostwald ripening occurred. In addition, the grain growth caused particle coarsening. Some grain boundaries remained without liquid penetration or

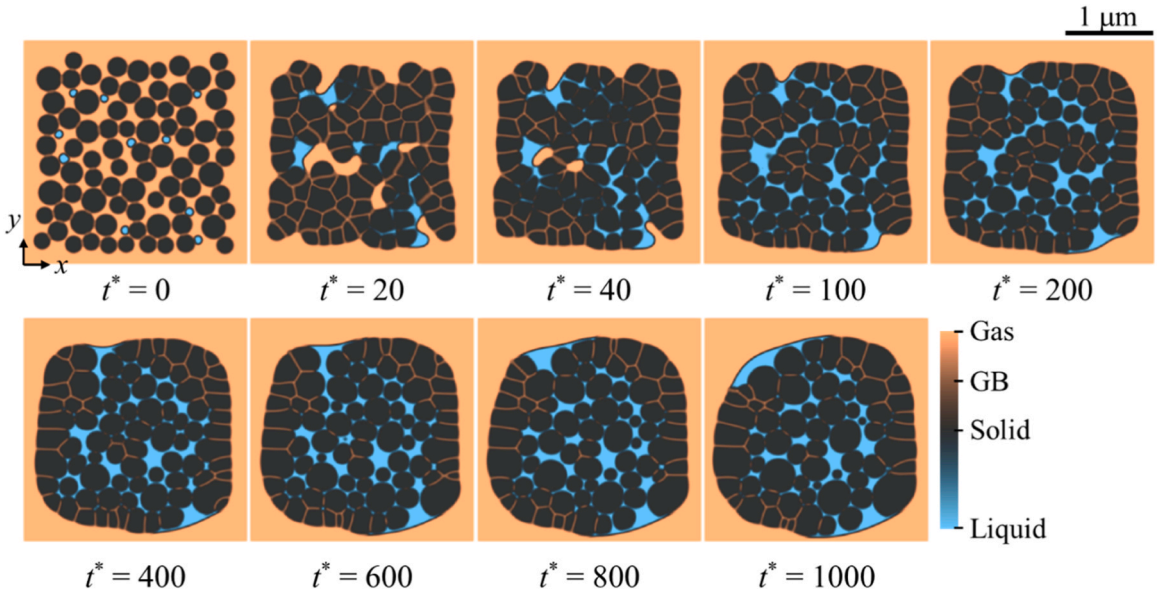

Fig. 10. Microstructural evolution obtained from the multi-phase-field simulation of liquid-phase sintering using 80 solid particles. Coarsening of solid particles via Ostwald ripening during the intermediate stage appears after $t^* = 100$.

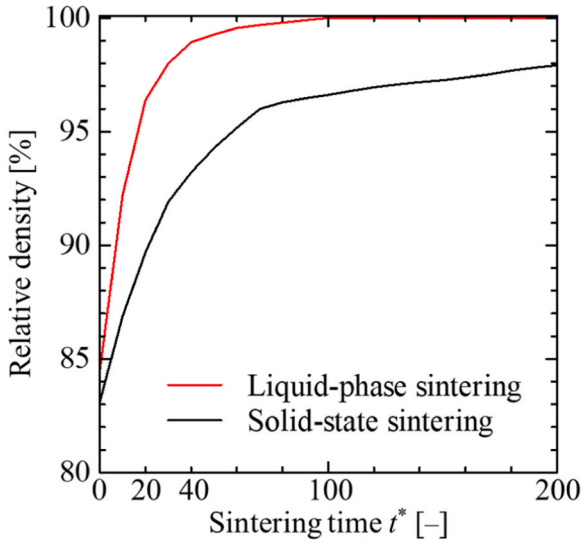

Fig. 11. Comparison of the relative densities between solid-state sintering and liquid-phase sintering calculated using the multi-phase-field simulation results up to $t^* = 200$.

were re-formed after separation. Around these grain boundaries, the necks grew because of solid-state bonding. Solid-state bonding led to RBM because the MPF model assumes that RBM is induced by grain boundary diffusion associated with neck growth. The three changes—contact flattening, Ostwald ripening, and solid-state bonding—are known to be the most significant mechanisms of microstructural evolution in LPS [2,3]. The developed MPF model reproduced the mechanisms simultaneously. From these results, the developed MPF model demonstrated that it can continuously simulate the microstructural evolution during LPS from the initial to final stages, with densification and grain coarsening manifested through Ostwald ripening and grain growth.

Fig. 12 shows the changes in concentration distributions from $t^* = 0$–100. The compositions of the solid and liquid phases were initially uniform, but after sintering started, c^A increased and c^B decreased in the liquid phases, and the opposite change occurred in the solid particles. These changes are reasonable and consistent with those predicted from the phase diagram shown in Fig. 1. Although the equilibrium values of c^C in the solid and liquid phases are equal, the concentration distributions of these phases are not uniform. The variation reflects the differences in diffusivity rates between the solid and liquid phases.

5. Conclusions

In this study, a new MPF model of sintering was developed based on the FID–MPF model by incorporating the advection term to simulate both SSS and LPS in multiphase and multicomponent systems, considering the RBM of the sintered particles. The developed MPF can be easily integrated with the CALPHAD database; it could therefore provide thermodynamically reasonable results of the phase transformation and solute diffusion during sintering. The following conclusions can be drawn from the MPF simulation results of SSS and LPS:

1) The SSS simulation results clarified that it is essential to consider the RBM to accurately predict the microstructural evolution during the SSS based on the MPF approach. The developed MPF model, which considers the RBM by calculating the advection term, can be used to analyze neck growth with an accuracy comparable to that of the well-established PF model of the SSS and reproduce the densification behavior independent of the compact size.
2) The LPS simulations using seven particles demonstrated that the proposed MPF model could reproduce the solubility relationships related to the densification behavior in the initial sintering stage. Moreover, the MPF simulations revealed that the RBM played an important role in explicitly describing the solid–liquid solubility relations.
3) The MPF model can continuously simulate the microstructural evolution during LPS from the initial to final stages. In the MPF simulations, the densification and grain coarsening were reproduced via three main mechanisms of microstructural evolution: contact flattening, Ostwald ripening, and solid-state bonding.

In future studies, the presented MPF model must be experimentally validated by comparing the simulation results obtained using an actual thermodynamic database from a material with the corresponding experimental results. Based on the validation, the presented MPF model of sintering provides a promising simulation for predicting the

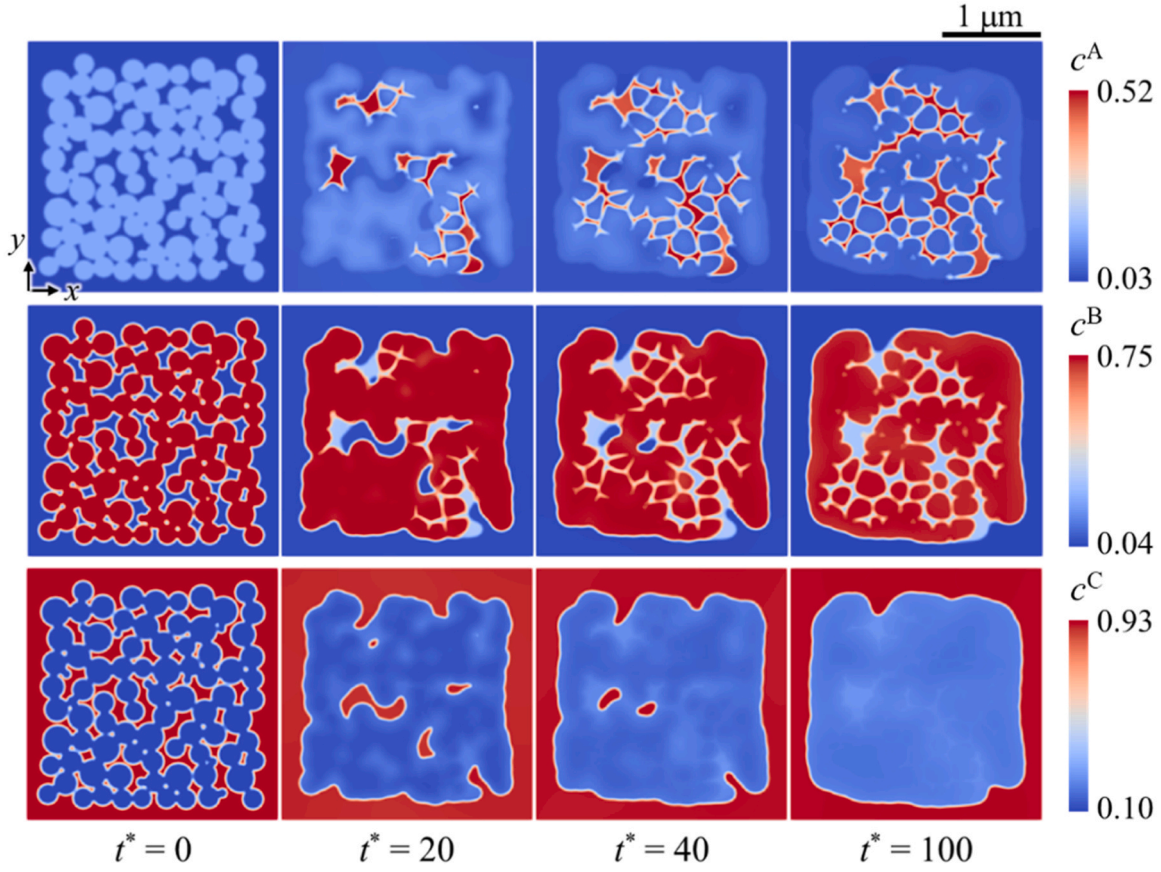

Fig. 12. Snapshots of the concentration distributions of the solute components A, B, and C, up to $t^* = 100$. c^A increases and c^B decreases in the regions corresponding to the liquid phases shown in Fig. 10.

microstructures of various sintered materials. Furthermore, the MPF model can provide more accurate predictions by coupling it with fluid dynamics.

Funding sources

This study was supported by the Materials Open Platform for Permanent Magnet in NIMS. It was also supported by the MEXT Program: Data Creation and Utilization-Type Material Research and Development Project (Digital Transformation Initiative Center for Magnetic Materials) [grant number JPMXP1122715503] and the Materials Processing Science Project Materealize of MEXT [grant number JPMXP0219207397]. A. Ishii acknowledges the International Center for Young Scientists (ICYS) at NIMS for providing ICYS fellowships.

CRediT authorship contribution statement

Akimitsu Ishii: Writing – original draft, Visualization, Validation, Software, Methodology, Investigation, Formal analysis, Data curation, Conceptualization. **Taichi Abe:** Writing – review & editing, Software, Resources, Methodology, Investigation, Funding acquisition. **Machiko Ode:** Writing – review & editing, Validation, Methodology, Investigation. **Toshiyuki Koyama:** Writing – review & editing, Supervision, Resources, Methodology, Investigation, Funding acquisition.

Declaration of Competing Interest

The authors declare that they have no known competing financial interests or personal relationships that could have appeared to influence the work reported in this paper.

Data availability

The data that has been used is confidential.

Appendix A. Advection in the concentration field

This section explains how advection is reflected in the time evolution of the concentration field c^i without adding an advection term to the time evolution equation of c^i_α. When the advection term acts on c^i, its time evolution can be expressed as

$$\frac{\partial c^i}{\partial t} = \frac{\partial c^i}{\partial t}_0 - \vartheta_c, \tag{A.1}$$

where $|_0$ indicates that the advection effect is not included in the term. ϑ_c represents the advection term with a dimension of $[s^{-1}]$. When Eq. (A.1) is solved using the explicit Euler method, the time-evolved concentration $c^{i'}$ obtained after Δt is given by the following equation:

$$c^{i'} = c^i + \left(\frac{\partial c^i}{\partial t}_0 - \vartheta_c\right)\Delta t = \left(c^i + \frac{\partial c^i}{\partial t}_0 \Delta t\right) - \vartheta_c \Delta t = c^{i'}{}_0 - \vartheta_c \Delta t. \tag{A.2}$$

Conversely, Eq. (2) yields the following equation:

$$c^{i'} = \sum_{\alpha=1}^{N} \phi'_\alpha c^{i'}_\alpha. \tag{A.3}$$

According to Eq. (9), the time evolution of ϕ_α can be calculated as follows:

$$\phi'_\alpha = \phi_\alpha + \left(\frac{\partial \phi_\alpha}{\partial t}_0 - \nabla\cdot\boldsymbol{v}_\alpha\right)\Delta t = \left(\phi_\alpha + \frac{\partial \phi_\alpha}{\partial t}_0 \Delta t\right) - (\nabla\cdot\boldsymbol{v}_\alpha)\Delta t = \phi'_\alpha 0 - (\nabla\cdot\boldsymbol{v}_\alpha)\Delta t \tag{A.4}$$

By substituting Eq. (A.4) to Eq. (A.3), the following equation is obtained:

$$\begin{aligned} c^{i'} &= \sum_{\alpha=1}^{N} \left(\phi'_\alpha 0 - (\nabla\cdot\boldsymbol{v}_\alpha)\Delta t\right) c^{i'}_\alpha \\ &= \sum_{\alpha=1}^{N} \phi'_\alpha 0 c^{i'}_\alpha - \sum_{\alpha=1}^{N} (\nabla\cdot\boldsymbol{v}_\alpha) c^{i'}_\alpha \Delta t \end{aligned}. \tag{A.5}$$

If the time evolution equation of c^i_α does not include the advection term, that is, $c^i_\alpha{}' = c^i_\alpha{}'|_0$, $c^{i'}$ can be written as

$$\begin{aligned} c^{i'} &= \sum_{\alpha=1}^{N} \phi'_\alpha 0 c^{i'}_\alpha 0 - \sum_{\alpha=1}^{N} (\nabla\cdot\boldsymbol{v}_\alpha) c^{i'}_\alpha \Delta t \\ &= c^{i'}{}_0 - \sum_{\alpha=1}^{N} (\nabla\cdot\boldsymbol{v}_\alpha) c^{i'}_\alpha \Delta t \end{aligned}. \tag{A.6}$$

By comparing Eqs. (A.2) and (A.7), ϑ_c can be obtained as follows:

$$\vartheta_c = \sum_{\alpha=1}^{N} (\nabla\cdot\boldsymbol{v}_\alpha) c^{i'}_\alpha. \tag{A.7}$$

Therefore, even if the advection term is not included in the time evolution of c^i_α, and if it is included in the time evolution of ϕ_α, the effect of advection can be reflected in the time evolution of c^i.

Appendix B. Investigation of the influence of permeability

To determine P^i used in this study, three PF simulations were performed using $P^{i*} = 0.1$, 1, and 10. A flat solid–liquid interface was set in the two-dimensional computational domain. The interface was fixed to focus on the changes in the concentration field. The initial molar fractions were uniformly set to $(c^A, c^B, c^C) = (0.75, 0.15, 0.1)$. The other conditions were the same as those described in Section 3. Fig. B.1 shows the distributions of c^A and c^B at the interface obtained from simulations with 1000 computational steps, which is quite low compared with the total number of computational steps used in the simulations described in the main text. The results demonstrate that if $P^i \geq 1$, the concentration distribution at the interface is unaffected by P^i, whereas if $P^i < 1$, the distribution is affected. Therefore, $P^i = 1$ was used in this study.

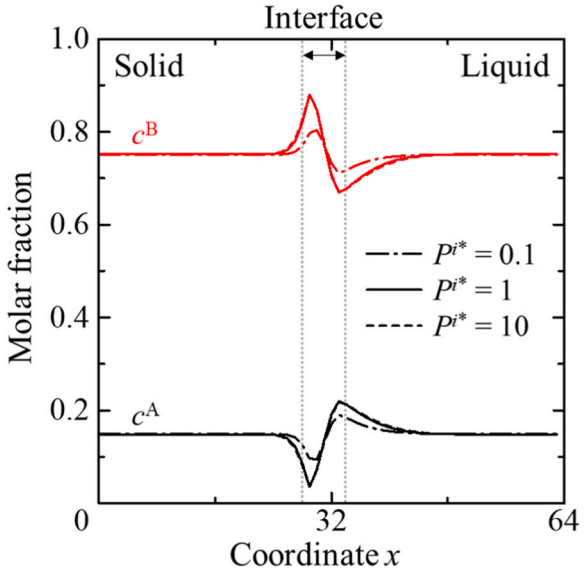

Fig. B.1. Distributions of the molar fractions c^A and c^B at the interface for the permeability $P^i = 0.1$, 1, and 10.

References

[1] R.M. German. Sintering: From Empirical Observations to Scientific Principles, first ed, Butterworth-Heinemann, Oxford, 2014.
[2] R.M. German, Plenum publishing corporation, New York, Liq. Phase Sinter. (1985).
[3] R.M. German, P. Suri, S.J. Park, Review: liquid phase sintering, J. Mater. Sci. 44 (2009) 1–39, https://doi.org/10.1007/s10853-008-3008-0.
[4] H. Sepehri-Amin, T. Ohkubo, T. Shima, K. Hono, Grain boundary and interface chemistry of an Nd–Fe–B-based sintered magnet, Acta Mater. 60 (2012) 819–830, https://doi.org/10.1016/j.actamat.2011.10.043.
[5] T.T. Sasaki, T. Ohkubo, K. Hono, Structure and chemical compositions of the grain boundary phase in Nd-Fe-B sintered magnets, Acta Mater. 115 (2016) 269–277, https://doi.org/10.1016/j.actamat.2016.05.035.
[6] J. Frenkel, Viscous flow of crystalline bodies under the action of surface tension, J. Phys. 9 (1945) 385–391.
[7] G.C. Kuczynski, Self-diffusion in sintering of metallic particles, JOM 1 (1949) 169–178, https://doi.org/10.1007/BF03398090.
[8] W.D. Kingery, M. Berg, Study of the initial stages of sintering solids by viscous flow, evaporation-condensation, and self-diffusion, J. Appl. Phys. 26 (1955) 1205–1212, https://doi.org/10.1063/1.1721874.
[9] R.L. Coble, Initial sintering of alumina and hematite, J. Am. Ceram. Soc. 41 (1958) 55–62, https://doi.org/10.1111/j.1151-2916.1958.tb13519.x.
[10] W.D. Kingery, Densification during sintering in the presence of a liquid phase. I. Theory, J. Appl. Phys. 30 (1959) 301–306, https://doi.org/10.1063/1.1735155.
[11] V.N. Eremenko, Y.V. Naidch, I.A. Lavrinenko, Liquid–Phase Sintering, Consultants Bureau, New York, 1970.
[12] R.L. Coble, Sintering crystalline solids. I. Intermediate and final state diffusion models, J. Appl. Phys. 32 (1961) 787–792, https://doi.org/10.1063/1.1736107.
[13] R.L. Coble, Sintering crystalline solids. II. Experimental test of diffusion models in powder compacts, J. Appl. Phys. 32 (1961) 793–799, https://doi.org/10.1063/1.1736108.
[14] S.-J.L. Kang, Y.-I. Jung, Sintering kinetics at final stage sintering: model calculation and map construction, Acta Mater. 52 (2004) 4573–4578, https://doi.org/10.1016/j.actamat.2004.06.015.
[15] M.F. Ashby, A first report on sintering diagrams, Acta Met. 22 (1974) 275–289, https://doi.org/10.1016/0001-6160(74)90167-9.
[16] J. Wang, R. Raj, Estimate of the activation energies for boundary diffusion from rate-controlled sintering of pure alumina, and alumina doped with zirconia or titania, J. Am. Ceram. Soc. 73 (1990) 1172–1175, https://doi.org/10.1111/j.1151-2916.1990.tb05175.x.
[17] M.-Y. Chu, M.N. Rahaman, L.C. De Jonghe, R.J. Brook, Effect of heating rate on sintering and coarsening, J. Am. Ceram. Soc. 74 (1991) 1217–1225, https://doi.org/10.1111/j.1151-2916.1991.tb04090.x.
[18] J.D. Hansen, R.P. Rusin, M.-H. Teng, D.L. Johnson, Combined-stage sintering model, J. Am. Ceram. Soc. 75 (1992) 1129–1135, https://doi.org/10.1111/j.1151-2916.1992.tb05549.x.
[19] C. Herring, Effect of change of scale on sintering phenomena, J. Appl. Phys. 21 (1950) 301–303, https://doi.org/10.1063/1.1699658.
[20] E.A. Olevsky, Theory of sintering: From discrete to continuum, Mater. Sci. Eng. R. Rep. 23 (1998) 41–100, https://doi.org/10.1016/S0927-796X(98)00009-6.
[21] Y.U. Wang, Computer modeling and simulation of solid-state sintering: a phase field approach, Acta Mater. 54 (2006) 953–961, https://doi.org/10.1016/j.actamat.2005.10.032.
[22] J. Hötzer, M. Seiz, M. Kellner, W. Rheinheimer, B. Nestler, Phase-field simulation of solid state sintering, Acta Mater. 164 (2019) 184–195, https://doi.org/10.1016/j.actamat.2018.10.021.
[23] I. Greenquist, M.R. Tonks, L.K. Aagesen, Y. Zhang, Development of a microstructural grand potential-based sintering model, Comput. Mater. Sci. 172 (2020) 109288, https://doi.org/10.1016/j.commatsci.2019.109288.
[24] R. Shi, M. Wood, T.W. Heo, B.C. Wood, J. Ye, Towards understanding particle rigid-body motion during solid-state sintering, J. Eur. Ceram. Soc. 41 (2021) 211–231, https://doi.org/10.1016/j.jeurceramsoc.2021.09.039.
[25] R. Zhang, Z. Chen, W. Fang, X. Qu, Thermodynamic consistent phase field model for sintering process with multiphase powders, Trans. Nonferrous Met. Soc. China 24 (2014) 783–789, https://doi.org/10.1016/S1003-6326(14)63126-5.
[26] W. Villanueva, K. Grönhagen, G. Amberg, J. Ågren, Multicomponent and multiphase simulation of liquid-phase sintering, Comput. Mater. Sci. 47 (2009) 512–520, https://doi.org/10.1016/j.commatsci.2009.09.018.
[27] H. Ravash, L. Vanherpe, J. Vleugels, N. Moelans, Three-dimensional phase-field study of grain coarsening and grain shape accommodation in the final stage of liquid-phase sintering, J. Eur. Ceram. Soc. 37 (2017) 2265–2275, https://doi.org/10.1016/j.jeurceramsoc.2017.01.001.
[28] A. Kazaryan, Y. Wang, B.R. Patton, Generalized phase field approach for computer simulation of sintering: Incorporation of rigid-body motion, Scr. Mater. 41 (1999) 487–492, https://doi.org/10.1016/S1359-6462(99)00179-7.
[29] V. Ivannikov, F. Thomsen, T. Ebel, R. Willumeit-Römer, Capturing shrinkage and neck growth with phase field simulations of the solid state sintering, Model. Simul. Mater. Sci. Eng. 29 (2021) 075008, https://doi.org/10.1088/1361-651X/ac1f87.
[30] F. Wakai, G. Okuma, Rigid body motion of multiple particles in solid-state sintering, Acta Mater. 235 (2022) 118092, https://doi.org/10.1016/j.actamat.2022.118092.
[31] F. Abdeljawad, D.S. Bolintineanu, A. Cook, H. Brown-Shaklee, C. Diantonio, D. Kammler, A. Roach, Sintering processes in direct ink write additive manufacturing: a mesoscopic modeling approach, Acta Mater. 169 (2019) 60–75, https://doi.org/10.1016/j.actamat.2019.01.011.
[32] Z. Zhao, X. Zhang, H. Zhang, H. Tang, Y. Liang, Numerical investigation into pressure-assisted sintering using fully coupled mechano-diffusional phase-field model, 111253, Int. J. Solids Struct. (2022) 234–235, https://doi.org/10.1016/j.ijsolstr.2021.111253.
[33] D. Choudhuri, L. Blake, Particle curvature effects on microstructural evolution during solid-state sintering: Phenomenological insights from phase-field simulations, J. Mater. Sci. 56 (2021) 7474–7493, https://doi.org/10.1007/s10853-021-05802-8.
[34] A. Ishii, K. Kondo, A. Yamamoto, A. Yamanaka, Phase-field modeling of solid-state sintering with interfacial anisotropy, Mater. Today Commun. 35 (2023) 106061, https://doi.org/10.1016/j.mtcomm.2023.106061.
[35] A. Ishii, A. Yamanaka, E. Miyoshi, Y. Okada, A. Yamamoto, Estimation of solid-state sintering and material parameters using phase-field modeling and ensemble four-dimensional variational method, Model. Simul. Mater. Sci. Eng. 29 (2021) 065012, https://doi.org/10.1088/1361-651X/ac13cd.
[36] S. Biswas, D. Schwen, J. Singh, V. Tomar, A study of the evolution of microstructure and consolidation kinetics during sintering using a phase field modeling based approach, Extrem. Mech. Lett. 7 (2016) 78–89, https://doi.org/10.1016/j.eml.2016.02.017.
[37] S. Biswas, D. Schwen, H. Wang, M. Okuniewski, V. Tomar, Phase field modeling of sintering: role of grain orientation and anisotropic properties, Comput. Mater. Sci. 148 (2018) 307–319, https://doi.org/10.1016/j.commatsci.2018.02.057.
[38] S. Biswas, D. Schwen, V. Tomar, Implementation of a phase field model for simulating evolution of two powder particles representing microstructural changes during sintering, J. Mater. Sci. 53 (2018) 5799–5825, https://doi.org/10.1007/s10853-017-1846-3.
[39] M. Seiz, Effect of rigid body motion in phase-field models of solid-state sintering, Comput. Mater. Sci. 215 (2022) 111756, https://doi.org/10.1016/j.commatsci.2022.111756.
[40] R. Termuhlen, X. Chatzistavrou, J.D. Nicholas, H.-C. Yu, Three-dimensional phase field sintering simulations accounting for the rigid-body motion of individual grains, Comput. Mater. Sci. 186 (2021) 109963, https://doi.org/10.1016/j.commatsci.2020.109963.
[41] W. Ma, Y. Shen, A phase field model for the solid-state sintering with parametric proper generalized decomposition, Powder Technol. 419 (2023) 118345, https://doi.org/10.1016/j.powtec.2023.118345.
[42] M. Plapp, Unified derivation of phase-field models for alloy solidification from a grand-potential functional, Phys. Rev. E Stat. Nonlin. Soft Matter Phys. 84 (2011) 031601, https://doi.org/10.1103/PhysRevE.84.031601.
[43] I. Greenquist, M. Tonks, M. Cooper, D. Andersson, Y. Zhang, Grand potential sintering simulations of doped UO_2 accident-tolerant fuel concepts, J. Nucl. Mater. 532 (2020) 152052, https://doi.org/10.1016/j.jnucmat.2020.152052.
[44] I. Steinbach, F. Pezzolla, A generalized field method for multiphase transformations using interface fields, Phys. D. 134 (1999) 385–393, https://doi.org/10.1016/S0167-2789(99)00129-3.
[45] S.G. Kim, W.T. Kim, T. Suzuki, Phase-field model for binary alloys, Phys. Rev. E Stat. Phys. Plasmas Fluids Relat. Interdiscip. Top. 60 (1999) 7186–7197, https://doi.org/10.1103/PhysRevE.60.7186.
[46] S.G. Kim, W.T. Kim, T. Suzuki, M. Ode, Phase-field modeling of eutectic solidification, J. Cryst. Growth 261 (2004) 135–158, https://doi.org/10.1016/j.jcrysgro.2003.08.078.
[47] J. Ågren, Calculation of phase diagrams: calphad, Curr. Opin. Solid State Mater. Sci. 1 (1996) 355–360, https://doi.org/10.1016/S1359-0286(96)80025-8.
[48] M. Segawa, A. Yamanaka, S. Nomoto, Multi-phase-field simulation of cyclic phase transformation in Fe-C-Mn and Fe-C-Mn-Si alloys, Comput. Mater. Sci. 136 (2017) 67–75, https://doi.org/10.1016/j.commatsci.2017.04.014.
[49] S. Nomoto, H. Wakameda, M. Segawa, A. Yamanaka, T. Koyama, Solidification analysis by non-equilibrium phase field model using thermodynamics data estimated by machine learning, Model. Simul. Mater. Sci. Eng. 27 (2019) 084008, https://doi.org/10.1088/1361-651X/ab3379.
[50] I. Steinbach, L. Zhang, M. Plapp, Phase-field model with finite interface dissipation, Acta Mater. 60 (2012) 2689–2701, https://doi.org/10.1016/j.actamat.2012.01.035.
[51] L. Zhang, I. Steinbach, Phase-field model with finite interface dissipation: Extension to multi-component multi-phase alloys, Acta Mater. 60 (2012) 2702–2710, https://doi.org/10.1016/j.actamat.2012.02.032.
[52] T. Koyama, Y. Tsukada, T. Abe, K. Kobayashi, Phase-field simulation on the formation of grain boundary phase in neodymium hard magnet, J. Jpn Inst. Met. Mater. 81 (2017) 43–48, https://doi.org/10.2320/jinstmet.JA201603.
[53] T. Nishizawa, Thermodynamics of Microstructures, ASM International, Ohio, 2008.
[54] L.E. Murr, Interfacial Phenomena in Metals and Alloys, Addison-Wesley, Massachusetts, 1975.